



HAL
open science

Stability analysis of a neural field self-organizing map

Georgios Is Detorakis, Antoine Chaillet, Nicolas P. Rougier

► **To cite this version:**

Georgios Is Detorakis, Antoine Chaillet, Nicolas P. Rougier. Stability analysis of a neural field self-organizing map. *Journal of Mathematical Neuroscience*, 2020, 10.1186/s13408-020-00097-6 . hal-03005121

HAL Id: hal-03005121

<https://inria.hal.science/hal-03005121>

Submitted on 13 Nov 2020

HAL is a multi-disciplinary open access archive for the deposit and dissemination of scientific research documents, whether they are published or not. The documents may come from teaching and research institutions in France or abroad, or from public or private research centers.

L'archive ouverte pluridisciplinaire **HAL**, est destinée au dépôt et à la diffusion de documents scientifiques de niveau recherche, publiés ou non, émanant des établissements d'enseignement et de recherche français ou étrangers, des laboratoires publics ou privés.

1 Stability analysis of a neural field self-organizing map

2 Georgios Is. Detorakis^{1, †}, Antoine Chaillet^{2,3, †}, and Nicolas P. Rougier^{4,5}

3 ¹adNomus Inc., San Jose, CA, USA

4 ²CentraleSupélec, Univ. Paris Saclay, Laboratoire des Signaux et Systèmes, Gif-sur-Yvette, France

5 ³Institut Universitaire de France

6 ⁴Inria Bordeaux Sud-Ouest, Bordeaux, France

7 ⁵Institut des maladies neurodégénératives, CNRS , Université de Bordeaux, France

8 [†]These authors contributed equally to this work

9 **Abstract** This work provides theoretical conditions guaranteeing that a self-organizing map efficiently
10 develops representations of the input space. The study relies on a neural fields model of spatiotemporal
11 activity in area 3b of the primary somatosensory cortex. We rely on Lyapunov’s theory for neural
12 fields to derive theoretical conditions for stability. The theoretical conditions are verified by numerical
13 experiments. The analysis highlights the key role played by the balance between excitation and inhibi-
14 tion of lateral synaptic coupling and the strength of synaptic gains in the formation and maintenance
15 of self-organizing maps.

16

17 **Keywords** self-organizing maps, neural fields, Lyapunov function, asymptotic stability, neural net-
18 works.

19 1 Introduction

20 Self-organizing maps (SOMs) are neural networks mapping a high-dimensional space to a low-
21 dimensional one, through unsupervised learning. They were first introduced by Grossberg (see [14] for
22 a review), and later by Kohonen [19]. SOMs are widely used in computer science and data analysis
23 for quantization and visualization of high dimensional data [37, 24]. They also constitute a suitable
24 tool in computational neuroscience to study the formation and maintenance of topographic maps in
25 primary sensory cortices such as the visual cortex [30, 23] and the somatosensory cortex [13, 33]. Many
26 variations and applications of Kohonen’s SOM algorithm can be found in [16] and [26].

27 A type of self-organizing map based on neural fields theory has been introduced in [8], where neural
28 fields are used to drive the self-organizing process. Neural fields are integrodifferential equations that
29 describe the spatiotemporal dynamics of a cortical sheet [3, 4, 5]. The SOM proposed in [8] describes
30 the topographic organization of area 3b of the primary somatosensory cortex of monkeys [21, 27]. The
31 model relies on an earlier work [28] known as Dynamic SOM (DSOM) algorithm. DSOM provides
32 an online SOM learning algorithm where the Kohonen’s SOM time-dependent learning rate and
33 neighborhood function have been replaced by time-invariant ones. DSOM’s neighborhood function and
34 learning rate solely depend on the distance of the winner unit (*i.e.*, the most active neuron) from the
35 input. The model proposed in [8, 9] combines the DSOM time-invariant learning rate and neighborhood
36 function with Oja’s learning rule [25]. As thoroughly described in [8, 9], the model is compatible
37 with anatomical evidence of how area 3b in monkeys develops, maintains and reorganizes topographic
38 representations of a skin patch of the index finger.

39 In this work, we provide theoretical insights on the stability and convergence of the neural field SOM
40 algorithm proposed in [8, 9] by studying a more general class of systems than the one proposed
41 originally in [8]. We use Lyapunov’s stability theory adapted to neural field dynamics [10]. Since
42 typical activation functions employed in the model (such as absolute values or rectification functions)
43 are not necessarily differentiable, we do not rely on linearization techniques but rather directly assess
44 the stability of the original nonlinear dynamics. Yet, the obtained results are local, meaning they are
45 valid only for initial conditions in the vicinity of the considered equilibrium. Nonetheless, we show
46 that they agree with numerical simulations. The stability conditions derived in this work can be used
47 towards the direction of tuning neural field models such that they achieve the best possible results in
48 developing self-organizing maps and thus more generalized representations. Moreover, the conditions

we propose indicate that the balance between lateral excitation and inhibition keeps the system stable, thus ruling out possible configurations in which learning does not take place properly. These findings are in line with both experimental observations [29, 18] and computational modeling [34, 35, 36].

The paper is organized as follows. In Section 2, we recall the SOM model under concern and its basic mechanisms. In Section 3, we present our main theoretical results, which we confront to numerical simulations in Section 4. A discussion on the obtained results is provided in Section 5. Mathematical proofs are given in Section 6.

2 Self-organizing neural fields

2.1 Neural population dynamics

We consider the following neural fields equation

$$\tau \frac{\partial u}{\partial t}(r, t) = -u(r, t) + \int_{\Omega} w_l(|r - r'|) \text{rect}(u(r', t)) dr' + I, \quad (1)$$

where Ω is a connected and compact subset of \mathbb{R}^q ($q = 1, 2, 3$). For $q = 2$, the integral of a function $g : \Omega = \Omega_1 \times \Omega_2 \rightarrow \mathbb{R}$ is to be understood as $\int_{\Omega} g(r) dr = \int_{\Omega_1} \int_{\Omega_2} g(r_1, r_2) dr_2 dr_1$ with $r = (r_1, r_2)$, and similarly for $q = 3$. $u(r, t)$ represents the mean membrane potential at position $r \in \Omega$ and time $t \geq 0$. τ is a positive decay time constant and I denotes an external input. w_l is a function that represents the strength of lateral synaptic coupling. It is given by

$$w_l(x) = w_e(x) - w_i(x), \quad (2)$$

where the excitation and inhibition synaptic weights are typically given by

$$w_e(x) = K_e e^{-x^2/2\sigma_e^2} \quad (3a)$$

$$w_i(x) = K_i e^{-x^2/2\sigma_i^2} \quad (3b)$$

with $K_e, K_i, \sigma_e, \sigma_i > 0$. In [8, 9], the input is provided through a two-dimensional skin model. The skin model is composed of a two-dimensional grid and receptors. The receptors are points distributed on the surface of the grid (uniformly). When a stimulus is applied on the grid, the receptors sample the input signal and convey the information to the cortical model. The skin stimulus is a noisy Gaussian-like function and the input to the neural fields model is provided by the following function I :

$$I(r, p, t) = 1 - \frac{|w_f(r, t) - s(p)|_1}{m}, \quad (4)$$

where $|\cdot|_1$ denotes the 1-norm: $|x|_1 = \sum_{i=1}^m |x_i|$, and $s : \mathbb{R}^2 \rightarrow [0, 1]^m$ is a function that maps the raw input from the two-dimensional skin space to $[0, 1]^m$. For instance, for a tactile stimulus at position $p \in \mathbb{R}^2$ on the skin, $s(p) \in \mathbb{R}^m$ could be defined as the normalized distance from p to each receptor's location, thus potentially of much higher dimension than 2. For a more detailed description of receptors' model please see [9]. $w_f : \Omega \times \mathbb{R}_{\geq 0} \rightarrow \mathbb{R}^m$ represents feed-forward synaptic weights whose value is updated according to

$$\frac{\partial w_f}{\partial t}(r, t) = \gamma (s(p) - w_f(r, t)) \int_{\Omega} w_e(|r - r'|) \text{rect}(u(r', t)) dr', \quad (5)$$

where γ is a positive constant that represents the learning rate and $\text{rect}(x) = \max\{x, 0\}$. It is worth observing that, since $s(p) \in [0, 1]^m$, $w_f(r, t) \in [0, 1]^m$ for all $r \in \Omega$ and all $t \geq 0$ given any **initial conditions satisfying $w_f(r, 0) \in [0, 1]^m$ for all $r \in \Omega$** (this can be seen by observing that the entries of $\frac{\partial w_f}{\partial t}(r, t)$ are negative as soon as the corresponding entries of $w_f(r, t)$ become greater than 1; similarly, they are positive when the corresponding entries of $w_f(r, t)$ get below 0: see (5)). Hence,

63 $\frac{|w_f(r,t)-s(p)|_1}{m} \in [0, 1]$ at all times. The expression (4) can thus be interpreted as a high input when the
 64 feedforward weights are close to $s(p)$ and a lower input when these are more distant.

65 The overall model Eq. (1, 4, 5) reflects the dynamics of a cortical neural population in combination
 66 with a learning rule of the feed-forward connections w_f , which convey information from receptors to the
 67 cortical sheet. As described in [8, 9], this model can express a variety of different behaviors, depending
 68 on the lateral connectivity kernels w_e and w_i .

69 The main advantage of the learning rule given by Eq. (5) is that it is a biologically plausible modification
 70 of the DSOM learning rule [28]. In DSOM the learning rate and neighborhood function are time-
 71 invariant and can adapt to the input according to one single parameter, called elasticity. This particular
 72 modification leads to the following behavior: if the winner neuron (*i.e.*, the neuron that has the shortest
 73 distance from the input stimulus to its corresponding codebook-weight) is close to the stimulus, then
 74 the neighborhood function shrinks around it. This results in making the weights of neurons within the
 75 dynamic neighborhood stronger and the weights of the other units weaker. However, when the winning
 76 unit is very far from the current input, the neighborhood function exhibits a broad activity pattern,
 77 promoting learning of every unit in the network. Therefore, in [8], the neighborhood function has been
 78 replaced by the term $\int_{\Omega} w_e(|r - r'|)\text{rect}(u(r', t))dr'$ providing a more realistic and biological plausible
 79 learning algorithm for self-organizing maps in the context of neuroscience.

80 2.2 Self-organizing maps

81 We start by briefly describing how the SOM model introduced in [8] and [9] works. The algorithm
 82 starts by initializing the feed-forward weights randomly (usually uniformly) and the neural field activity
 83 $u(r, 0)$ is set to zero. The second step is to sample the input space by randomly drawn samples of
 84 dimension m from an input distribution. At every epoch one sample is given to the neural field Eq. (1)
 85 and (5) through Eq. (4). This first step is depicted in Figure 1 **A**, where a two-dimensional point
 86 $p = (p_1, p_2)$ is sampled from a uniform distribution $p_1, p_2 \sim \mathcal{U}(0, 1)$. The samples are mapped to the
 87 neural space through the function s and then are passed to Eq. (4). At this point we should point
 88 out that there are two ways of presenting stimuli while training a self-organizing map. The first is to
 89 predetermine an amount of input samples and present one at each epoch (on-line learning) and the
 90 second is to collect all the input samples into a batch and give all of them at once to the network
 91 (batch learning). In this work we use the former (on-line learning) since it is biologically **plausible**.

92 Then the algorithm proceeds with computing the numerical solution of Eq. (1) and (5). To that
 93 aim, Eq. (1) and Eq. (5) are discretized and solved numerically using Euler's forward method. The
 94 numerical solution of Eq. (1) is typically a bell-shaped curve (bump) centered on the neuron which
 95 is the closest unit to the input sample and therefore is called winner neuron or best matching unit
 96 (BMU). In Figure 1**B** this is depicted as a black disc on a discrete lattice. The lattice represents a
 97 discretization of the field where each tile corresponds to a neuron. Neurons that lie within the vicinity
 98 (within the black disc in Figure 1 **B**) defined by the solution of Eq. (1) update their weights based
 99 on Eq. (5). The rest of the neurons feed-forward weights remain in their previous state. Once the
 100 temporal integration of Eq. (1) and Eq. (5) is complete the activity of the field is reset to its baseline
 101 activity. Then another input sample is drawn and the whole process repeats itself. Once the number
 102 of epochs has been exhausted, the learning stops and the mapping process has been completed.

103 To make the aforementioned algorithm directly comparable to Kohonen SOM [19] we provide some
 104 insights. First, in Kohonen's SOM we compute the distance between the input and the codebooks.
 105 Here we do the same using Eq. (4). The neighborhood function that Kohonen's SOM uses to update
 106 the feed-forward weights is replaced here by the numerical solution of the neural field (Eq. (1)) and
 107 more precisely by the term $\int_{\Omega} w_e(|r - r'|)\text{rect}(u(r', t))dr'$. Both the learning rate and the width of the
 108 neighborhood function are time-independent in our case as opposed to Kohonen's SOM where they
 109 are both time-dependent. Our learning rule is different since we use a modified Oja rule [25], which
 110 is based on Hebbian learning [15] and it is therefore biologically plausible [1]. The dimensionality
 111 reduction in both models, the Kohonen and ours, takes place at the level of the learning rule. This
 112 means that Eq. (5) is responsible for learning the representations and mapping the input distribution

113 (of dimensions m) on a manifold of lower dimension $q \in \{1, 2, 3\}$.

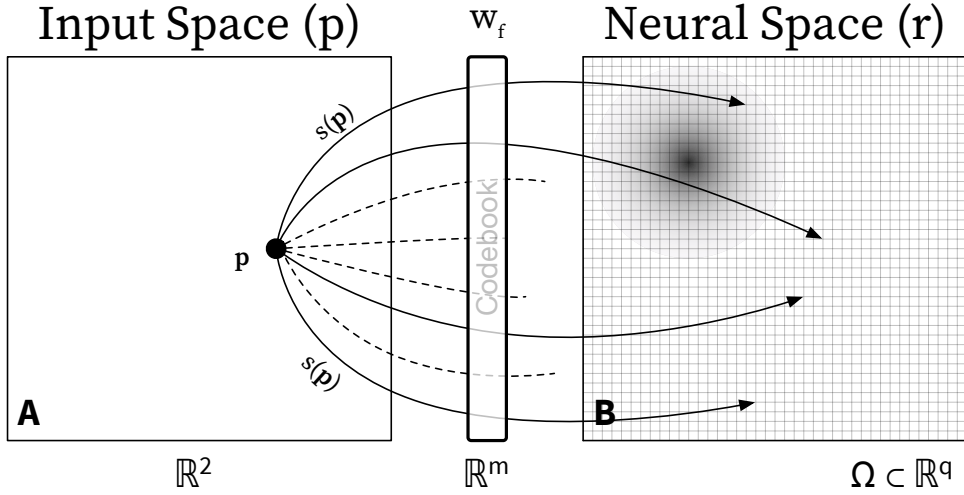


Figure 1: **Neural field self-organizing map.** Graphical representation of the learning algorithm introduced in [8, 9]. **A** Tactile bi-dimensional stimuli are mapped to an m -dimensional space through a function s that involves the skin receptors. This function is used to update the codebooks, which are then mapped to the neural space Ω of lower dimension. The input I receives the mapped input sample and provides input to the neural field and codebooks equations. **B** The numerical steady-state solution of Eq. (1) (*i.e.*, bump) defines the neighborhood (the group of neurons) that will have its neurons updating their codebooks based on Eq. (5).

114 3 Explicit conditions for stability

115 The most important question when one trains a self-organizing map is: *Will the learning process*
 116 *converge and properly map the input space to the neural one?* In most of the cases, it is not possible to
 117 predict this. However, in the specific case of the self-organizing algorithm provided by [8], we show
 118 here that it is possible to obtain an analytical condition that guarantee the stability of the equilibrium
 119 point of system (1)-(5). Stability during learning is a pre-requisite to generate a meaningful mapping
 120 and thus a proper topographic map. Moreover, a byproduct of deriving such a stability condition is to
 121 provide some insights on how to properly tune model parameters.

122 To this end, we now proceed to the mathematical analysis of the model. For the sake of generality, the
 123 adopted mathematical framework is slightly wider than merely Eq. (1, 4, 5) and encompasses more
 124 general classes of activation functions and synaptic kernels. We start by introducing the considered
 125 class of systems, and then provide sufficient conditions for its stability and convergence.

126 3.1 Model under study

The self-organizing neural field Eq. (1, 4, 5) is a particular case of the more general dynamics

$$\tau \frac{\partial u}{\partial t}(r, t) = -u(r, t) + \int_{\Omega} w_l(r, r') f_l(u(r', t)) dr' + f_s(w_f(r, t) - s(p)) \quad (6a)$$

$$\frac{\partial w_f}{\partial t}(r, t) = \gamma (s(p) - w_f(r, t)) \int_{\Omega} w_e(r, r') f_e(u(r', t)) dr', \quad (6b)$$

127 where $\tau, \gamma > 0$, $w_l, w_e \in L_2(\Omega^2, \mathbb{R})$, the set of all square-integrable functions from Ω^2 to \mathbb{R} , and f_e, f_l
 128 and f_s are Lipschitz continuous functions.

129 3.2 Existence of equilibrium patterns

Assuming that $\inf_{r \in \Omega} \int_{\Omega} w_e(r, r') f_e(u^*(r')) dr' \neq 0$, any equilibrium pattern (u^*, w_f^*) of (6) satisfies the following equations:

$$u^*(r) = f_s(0) + \int_{\Omega} w_l(r, r') f_l(u^*(r')) dr' \quad (7a)$$

$$w_f^*(r) = s(p). \quad (7b)$$

130 Since $w_l \in L_2(\Omega^2, \mathbb{R})$, [11, Theorem 3.6] ensures the existence of at least one such equilibrium pattern.

131 3.3 Stability analysis of Eq. (6)

We recall that an equilibrium x^* of a system $\dot{x}(t) = f(x(t))$, where $x(t) : \Omega \rightarrow \mathbb{R}^n$ for each fixed $t \geq 0$, is called *globally exponentially stable* if there exist $k, \varepsilon > 0$ such that, for all admissible initial conditions, it holds that

$$\|x(t) - x^*\| \leq k \|x(0) - x^*\| e^{-\varepsilon t}, \quad \forall t \geq 0, \quad (8)$$

132 where $\|\cdot\|$ denotes the spatial L_2 -norm. This property thus ensures that all solutions go to the
 133 equilibrium configuration x^* in the L_2 sense (global convergence), and that the transient overshoot
 134 is proportional to the L_2 -norm of the distance between the initial configuration and the equilibrium
 135 (stability). The equilibrium pattern x^* is said to be *locally exponentially stable* if (8) holds only for
 136 solutions starting sufficiently near from it (in the L_2 sense). We refer the reader to [10] for a deeper
 137 discussion on the stability analysis of neural fields.

138 Our main result proposes a sufficient condition for the local exponential stability of Eq. (6). Its proof
 139 is given in Section 6.1.

Theorem 1. *Let Ω be a compact connected set of \mathbb{R}^d , $w_l \in L_2(\Omega^2, \mathbb{R})$ and $w_e : \Omega^2 \rightarrow \mathbb{R}$ be a bounded function. Assume further that f_l, f_s and f_e are Lipschitz continuous functions, and let ℓ_l denote the Lipschitz constant of f_l . Let (u^*, w_f^*) denote any equilibrium of Eq. (6), as defined in Eq. (7). Then, under the conditions that*

$$\sqrt{\int_{\Omega} \int_{\Omega} w_l(r, r')^2 dr' dr} < \frac{1}{\ell_l} \quad (9)$$

$$\inf_{r \in \Omega} \int_{\Omega} w_e(r, r') f_e(u^*(r')) dr' > 0, \quad (10)$$

140 *the equilibrium pattern (u^*, w_f^*) is locally exponentially stable for Eq. (6).*

141 Condition (9) imposes that the synaptic weights of the lateral coupling w_l be sufficiently small: stronger
 142 lateral synaptic weights can be tolerated if the maximum slope ℓ_l of the activation function f_l is
 143 low enough, meaning that the system given by Eq. (6a) is less self-excitable. Recall that, if f_l is a
 144 differentiable function, then ℓ_l can be picked as the maximum value of its derivative. Nonetheless,
 145 Theorem 1 does not impose such a differentiability requirement, thus allowing to consider non-smooth
 146 functions such as absolute values, saturations, or rectification functions. Note that it was shown in [32]
 147 that condition (9) ensures that the system owns a single equilibrium pattern. It is also worth stressing
 148 that the slopes of the functions f_s and f_e do not intervene in the stability conditions.

149 Condition (10) requires a sufficient excitation in the vicinity of the equilibrium u^* . Roughly speaking,
 150 it imposes that the considered equilibrium pattern u^* does not lie in a region where f_e is zero.

151 3.4 Stability analysis of the SOM neural fields

Theorem 1 provides a stability condition for the model described by Eq. (6). We next apply it to the model given in [8] in order to derive more explicit and testable stability conditions. More

precisely, the self-organizing neural fields Eq. (1, 4, 5) can be put in the form of Eq. (6) by letting $f_e(x) = f_l(x) = \text{rect}(x)$, $f_s(x) = 1 - \frac{|x|_1}{m}$ and

$$w_e(r, r') = K_e e^{-|r-r'|^2/2\sigma_e^2} \quad (11a)$$

$$w_i(r, r') = K_i e^{-|r-r'|^2/2\sigma_i^2} \quad (11b)$$

$$w_l(r, r') = w_e(r, r') - w_i(r, r'). \quad (11c)$$

In view of (7), the equilibrium patterns of Eq. (1, 4, 5) are given by

$$u^*(r) = 1 + \int_{\Omega} w_l(r, r') \text{rect}(u^*(r')) dr' \quad (12a)$$

$$w_f^*(r) = s(p). \quad (12b)$$

152 The Lipschitz constant of f_l is $\ell_l = 1$. Based on this, we can also derive the following corollary, whose
153 proof is provided in Section 6.2.

Corollary 1. *Assume that Ω is a compact and connected set of \mathbb{R}^q and let w_e , w_i and w_l be as in (11). Then, under the condition that*

$$\int_{\Omega} \int_{\Omega} \left(K_e e^{-|r-r'|^2/2\sigma_e^2} - K_i e^{-|r-r'|^2/2\sigma_i^2} \right)^2 dr' dr < 1, \quad (13)$$

154 *the equilibrium (u^*, w_f^*) , as defined in Eq. (12), is locally exponentially stable for Eq. (1)-(5).*

155 A particular case for which local exponential stability holds is when the excitation and inhibition weight
156 functions are sufficiently balanced. Indeed, it appears clearly that Eq. (13) is fulfilled if $K_e \simeq K_i$ and
157 $\sigma_e \simeq \sigma_i$. See the discussion in Section 5 for further physiological insights on this condition.

158 The integral involved in (13) can be solved explicitly. For instance, in the two-dimensional case ($q = 2$),
159 the condition boils down to the following.

Corollary 2. *Assume that $\Omega = [a, b] \times [a, b]$ for some $a, b \in \mathbb{R}$ with $b \geq a$ and let w_e , w_i and w_l be as in (11). Define*

$$\xi_{a,b}(\sigma) := \left(2\sigma^2 \left(e^{-\frac{(a-b)^2}{2\sigma^2}} - 1 \right) + \sigma\sqrt{2\pi}(a-b)\text{Erf}\left(\frac{a-b}{\sigma\sqrt{2}}\right) \right)^2, \quad \forall \sigma > 0, \quad (14)$$

where $\text{Erf}: \mathbb{R} \rightarrow (-1, 1)$ denotes the Gauss Error Function. Then, under the condition that

$$K_e^2 \xi_{a,b}(\sigma_e/\sqrt{2}) + K_i^2 \xi_{a,b}(\sigma_i/\sqrt{2}) - 2K_e K_i \xi_{a,b}\left(\frac{\sigma_e \sigma_i}{\sqrt{\sigma_e^2 + \sigma_i^2}}\right) < 1, \quad (15)$$

160 *the equilibrium (u^*, w_f^*) , as defined in Eq. (12), is locally exponentially stable for Eq. (1)-(5).*

Plenty of approximations are available for the Erf function in the literature. For instance, the following expression approximates it with a 5.10^{-4} error:

$$\text{Erf}(x) \simeq 1 - \frac{1}{(1 + a_1 x + a_2 x^2 + a_3 x^3 + a_4 x^4)^4},$$

161 with $a_1 = 0.278393$, $a_2 = 0.230389$, $a_3 = 0.000972$, $a_4 = 0.078108$; see for instance [2]. The Erf function
162 is also commonly implemented in mathematical software, thus making Eq. (15) easily testable in
163 practice.

4 Numerical assessment on a two-dimensional map

In order to numerically assess whether the above stability condition correctly predicts the performance of the learning process, we focus on a simple example of a two-dimensional map ($q = 2$) and a two-dimensional input space ($n = 2$). Furthermore, we choose $s(p)$ to be the identity function since we do not consider any receptors: the position of the tactile stimuli is assumed to be directly available. This choice is motivated by the fact that the presence or absence of a receptors grid does not affect the theoretical results of the current work. We refer to [8, 9] for a more complex application of the neural field self-organizing algorithm.

We sample two-dimensional inputs from a uniform distribution. Therefore we have $s_i(p) = (p_1, p_2)$ where i indicates the i -th sample, and $p_1, p_2 \sim \mathcal{U}(0, 1)$. In all our simulations we use 7000 sample points and we train the self-organizing map over each of them (7000 epochs). It is worth stressing the difference between the training time (epochs) and the simulation time. The former refers to the iterations over all the input samples (stimuli): one such input is presented to the model at each epoch. The latter is attributed to the numerical temporal integration of Eq. (1)-(5). Each epoch thus corresponds to a predefined number of simulation steps. At the end of each epoch the activity of the neural field is reset to baseline activity before proceeding to the next epoch.

4.1 Parameters and simulation details

The neural fields equations are discretized using $k = 40 \times 40$ units. Accordingly, the two-dimensional model Eq. (1)-(5) is simulated over a spatial uniform discretization Ω_d of the spatial domain $\Omega = [0, 1] \times [0, 1]$, namely $\Omega_d = \bigcup_{i,j=1}^{40} (\frac{i}{40}, \frac{j}{40})$. The considered input space, over which the stimuli are uniformly distributed, is also $[0, 1] \times [0, 1]$ (two-dimensional input vectors). The temporal integration is performed using the forward Euler method, whereas the spatial convolution in Eq. (1)-(5) is computed via the Fast-Fourier Transform (FFT). The learning process runs for 7000 epochs. The components of the feed-forward weights are initialized from a uniform distribution $\mathcal{U}(0, 0.01)$ and the neural field activity is set to zero. At each epoch, we feed a stimulus to Eq. (1)-(5) and the system evolves according to its dynamics while the feed-forward weights are being updated. Then we reset the neural fields activity to zero. We run each experiment ten times using a different pseudo-random number generator (PRNG) seed each time (the PRNG seeds are given in Appendix 6.3: the same initial conditions and set of PRNG seeds sequence were used in each experimental condition).

The source code is written in Python (Numpy-, Numba-, Sklearn, and Matplotlib-dependent) and are freely distributed under the GPL 3-Clause License (https://github.com/gdetor/som_stability). All the parameters used in numerical simulations are summarized in Table 1. All simulations ran on an Intel NUC machine equipped with an Intel i7-10th generation processor and 32 GB of physical memory, running Ubuntu Linux (20.04.1 LTS, Kernel: 5.4.0-47-generic). The simulation of one self-organizing map consumes 493 MB of physical memory and it took 2671 seconds to run the 7000 epochs.

	K_e	σ_e	K_i	σ_i	τ	dt	t	γ	epochs
Figure 2	0.90	0.11	0.86	1.0	1.0	0.015	25.0	0.002	7000
Figure 3	3.0	0.11	2.80	1.0	1.0	0.015	25.0	0.002	7000

Table 1: **Simulation parameters.** K_e and K_i are the amplitudes of excitatory and inhibitory lateral connections, respectively. σ_e and σ_i are the variances of excitatory and inhibitory lateral connections, respectively. τ is the decay time constant, dt is the integration time step in ms, t is the simulation time in seconds. γ is the learning rate. In each epoch one stimulus is presented to the model.

4.2 SOM's quality measures

We measure the quality of the self-organizing maps using two performance indicators: the distortion \mathcal{D} [6] and the $\delta x - \delta y$ representation [7]. We recall here that Ω_d is the spatial uniform discretization of $\Omega = [0, 1] \times [0, 1]$ and $k = 40 \times 40$ is the number of nodes (neurons). Furthermore, for each

203 $j \in \{1, \dots, k\}$, $w_f^j(t^*)$ denotes the steady-state value of the feed-forward weights at the j -th node of
 204 the spatial discretization and t^* corresponds to the time at the end of an epoch.

The distortion assesses the quality of a self-organizing map. It measures the loss of information over the learning process. In other words, it indicates how good a reconstruction of an input will be after the mapping of all inputs to a lower-dimensional neural map. In a sense, distortion measures how well a SOM algorithm “compresses” the input data with respect to the neighborhood structure. Mathematically, the distortion is computed according to its discrete approximation

$$\mathcal{D} = \frac{1}{n} \sum_{i=1}^n \min_{j \in \{1, \dots, k\}} |s_i(p) - w_f^j(t^*)|^2, \quad (16)$$

205 where n is the number of samples we use during the training of the self-organizing map.

206 Distortion is essentially an indicator of the map convergence, but it is not a reliable tool for assessing
 207 its quality. To gauge the quality of the map, we use the $\delta x - \delta y$ representation [7]. It shows when a
 208 map preserves the topology of the input space and hence how well a topographic map is formed. In
 209 order to estimate the $\delta x - \delta y$, we compute all the pairwise distances between the feed-forward weights,
 210 $\delta x = \delta x(i, j) = |w_f^i(t^*) - w_f^j(t^*)|$, and all the distances between the nodes of the uniform discretization
 211 of the input space $[0, 1]^2$, $\delta y(i, j) = |y_i - y_j|$, for each $i, j = 1, \dots, k$, where y_i are the discrete nodes of
 212 Ω_d . We plot the $\delta x - \delta y$ (*i.e.*, δx is the ordinate and δy the abscissa) along with a straight line, named
 213 $\mathcal{L}_{\delta x - \delta y}$, that crosses the origin and the mean of δx points. If the point cloud representation of $\delta x - \delta y$
 214 closely follows the line $\mathcal{L}_{\delta x - \delta y}$ then the map is considered well-formed and preserves the topology of
 215 the input space.

216 In order to quantify the $\delta x - \delta y$ representation through a scalar performance index, we perform a linear
 217 regression on the point cloud of $\delta x - \delta y$ without fitting the intercept (magenta line in figures) and we
 218 get a new line named \mathcal{L}_Δ . Then we define the measure $\mathcal{P} = \sqrt{\sum_{i=1}^k (a_i - b_i)^2}$, where $a_i \in \mathcal{L}_{\delta x - \delta y}$, and
 219 $b_i \in \mathcal{L}_\Delta$. Naturally, \mathcal{P} should approach zero as the two lines are getting closer, indicating that the
 220 self-organizing map respects the topology of the input space and thus it is well-formed.

221 4.3 Stable case

222 We start by simulating the model described by Eq. (1)-(5) with the parameters given in first line of
 223 Table 1. With these parameters, Condition (15) is fulfilled ($0.47 < 1$) and Corollary 2 predicts that the
 224 equilibrium is exponentially stable over each epoch. Accordingly, the model succeeds in building up a
 225 self-organizing map as shown in panel **A** of Figure 2. The white discs indicate the feed-forward weights
 226 after learning and the black dots indicate the input data points (two-dimensional rectangular uniform
 227 distribution).

228 Panels **B** and **C** show the $\delta x - \delta y$ representation and the distortion, respectively. We observe that the
 229 $\delta x - \delta y$ representation indicates a correlation between the feed-forward weights and the rectangular grid
 230 points (aligned with the mean of δx —red line). This means that the self-organizing map is well-formed
 231 and conserves the topology of the input. Moreover, the distortion declines and converges towards
 232 0.0025 pointing out first that the loss of information during learning is low and that the structure in
 233 the self-organizing map is preserved. However, the boundary effects (the density of points is higher
 234 at the boundary of the map in panel **A**) affect both the distortion (it does not converge to zero – see
 235 panel **C** in Figure 2) and the $\delta x - \delta y$ representation (it is not perfectly aligned with the red line – see
 236 panel **B** in Figure 2). In spite of these boundary effects, the obtained $\delta x - \delta y$ performance indicator is
 237 good ($\mathcal{P} = 0.01$).

238 The evolution of the norm-2 of feed-forward weights of three randomly chosen units ($r^* = (0.25, 0.25)$,
 239 $(0.1, 0.225)$, $(0.35, 0.075)$) is shown in the panel **D** of Figure 2. This implies that the weights converge
 240 to an equilibrium after a transient period of about 2000 epochs. The oscillations around the equilibrium
 241 are due to a repeated alteration of the input stimulus which causes a shift to the feed-forward weights
 242 values of each winner neuron (see [8] for more details).

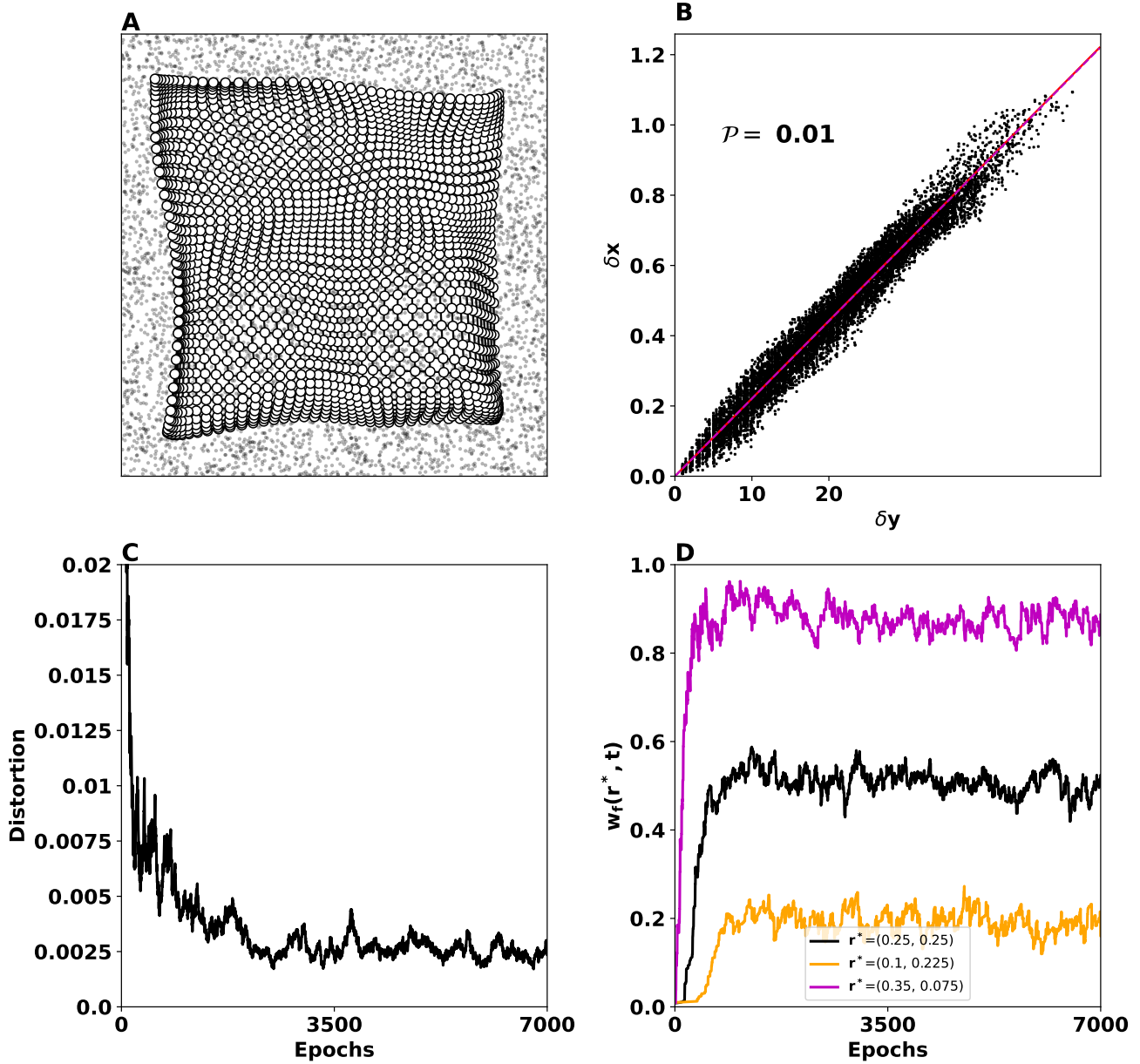


Figure 2: **Two-dimensional SOM performance in the stable case.** **A** Feed-forward weights (white discs) as they have been organized into a topographic map after 7000 epochs. The input in this case is a two-dimensional rectangular uniform distribution (black dots). **B** $\delta x - \delta y$ representation (black cloud), mean of δx (red line), and the linear regression of the $\delta x - \delta y$ representation (magenta line). The fact that the cloud is aligned around the red line indicates that the topographic map is well-organized, as confirmed by a good index performance $\mathcal{P} = 0.01$. **C** Distortion indicates that the loss of information during the learning process decreases and the mapping of the input data to a two-dimensional self-organizing map respects the structure of the neighborhoods. **D** Temporal evolution of norm-2 of feed-forward weights of three neurons placed at $r^* = (0.25, 0.25)$, $(0.1, 0.225)$, and $(0.35, 0.075)$. Condition (15) is fulfilled and therefore the weights converge to an equilibrium giving rise to a well-formed topographic map.

243 4.4 Unstable case

244 The second line of Table 1 provides parameters for which Condition (15) is violated ($5.25 > 1$).
245 According to our theoretical predictions, the model might not be stable and thus may not be able to
246 develop any self-organizing map at all. In order to make sure that this is the case (and not merely a
247 transient effect), we have let the training take more epochs (20 000). Nevertheless, we present here only
248 the 7 000 first epochs for consistency with the rest of our experiments. This situation is illustrated in
249 Figure 3, where the self-organizing process has failed to generate a well-formed map (panel **A**). In this
250 case it is apparent that self-organization process has failed to generate a topographic map.

251 The $\delta x - \delta y$ representation in panel **B** of Figure 3 looks like a diffused cloud, indicating that there is no
252 correlation between the grid points and the feed-forward weights meaning that there is no preservation
253 of the topology of the input space. Accordingly the performance index reaches the value $\mathcal{P} = 0.41$, thus
254 higher than the stable case. Moreover, the distortion in panel **C** of Figure 3 oscillates without converging
255 to an equilibrium pointing out that the loss of information remains high and therefore the mapping is
256 not successful. Finally, the norm-2 of feed-forward weights of three units ($r^* = (0.25, 0.25), (0.1, 0.225),$
257 $(0.35, 0.075)$) are shown in panel **D**: it is apparent that they do not converge to an equilibrium. Instead
258 they oscillate violently and they never stabilize around an equilibrium configuration.

259 4.5 Numerical Assessment of Corollary 2

260 Finally, we numerically tested Condition (15) of Corollary 2 for different values of the parameters K_e
261 and K_i (all other parameters remained the same as in Table 1). For each pair (K_e, K_i) we computed
262 the left-hand side of Eq. (15), the distortion \mathcal{D} (averaged over the last 10 epochs), and the $\delta x - \delta y$
263 performance index \mathcal{P} : see Figure 4. We observe that, for high values of K_e and K_i , the stability
264 condition of Corollary 2 is violated (the black solid line overpasses the black dashed line). The distortion
265 (orange curve) closely follows the left-hand side of Condition (15) (up to a scaling factor), suggesting
266 that distortion can serve as a measure of stability of the system (1)-(5). Furthermore, the distortion
267 and the $\delta x - \delta y$ performance index \mathcal{P} indicate that the learning process degrades for high values of
268 (K_e, K_i) , in line with the fact that Condition (15) is violated. Figure 5 confirms this good alignment
269 between the theoretical stability condition and the performance of the self-organizing map: for the first
270 five cases it properly maps the input space to the neural one, whereas the topology of the input space
271 is not preserved in the last two cases and a malformed topographic map is obtained.

272 5 Conclusion

273 In this work, we have presented theoretical conditions for the stability of a neural fields system coupled
274 with an Oja-like learning rule [25]. Numerical assessments on a two-dimensional self-organizing map
275 indicate that the theoretical condition is closely aligned with the capacity of the network to form a
276 coherent topographic map.

277 Previous works have shown through simulations that the dynamical system described by Eq. (1)-(5)
278 can develop topographic maps through an unsupervised self-organization process [8, 9]. The model
279 relies on the activity of a neural field to drive a learning process. This type of models are capable of
280 developing topographic maps and reorganize them in face of several kinds of disturbances. Here, we
281 proceed to a rigorous theoretical analysis of such kind of models by employing neural fields Lyapunov
282 theory.

283 The obtained stability conditions are reminiscent of those obtained for general neural fields dynamics,
284 in which the spatial L_2 -norm of synaptic weights plays an essential role [10, 32, 12]. In our setting,
285 these conditions translate in a good balance between excitation and inhibition for the exponential
286 stability of the model's equilibrium, thus allowing the self-organizing process to develop topographic
287 maps. It is worth stressing that the proof techniques employed here do not rely on a linearization of
288 the system around the considered equilibrium; it thus allows to cover activation functions that are not
289 differentiable (such as classical saturation or rectification functions).

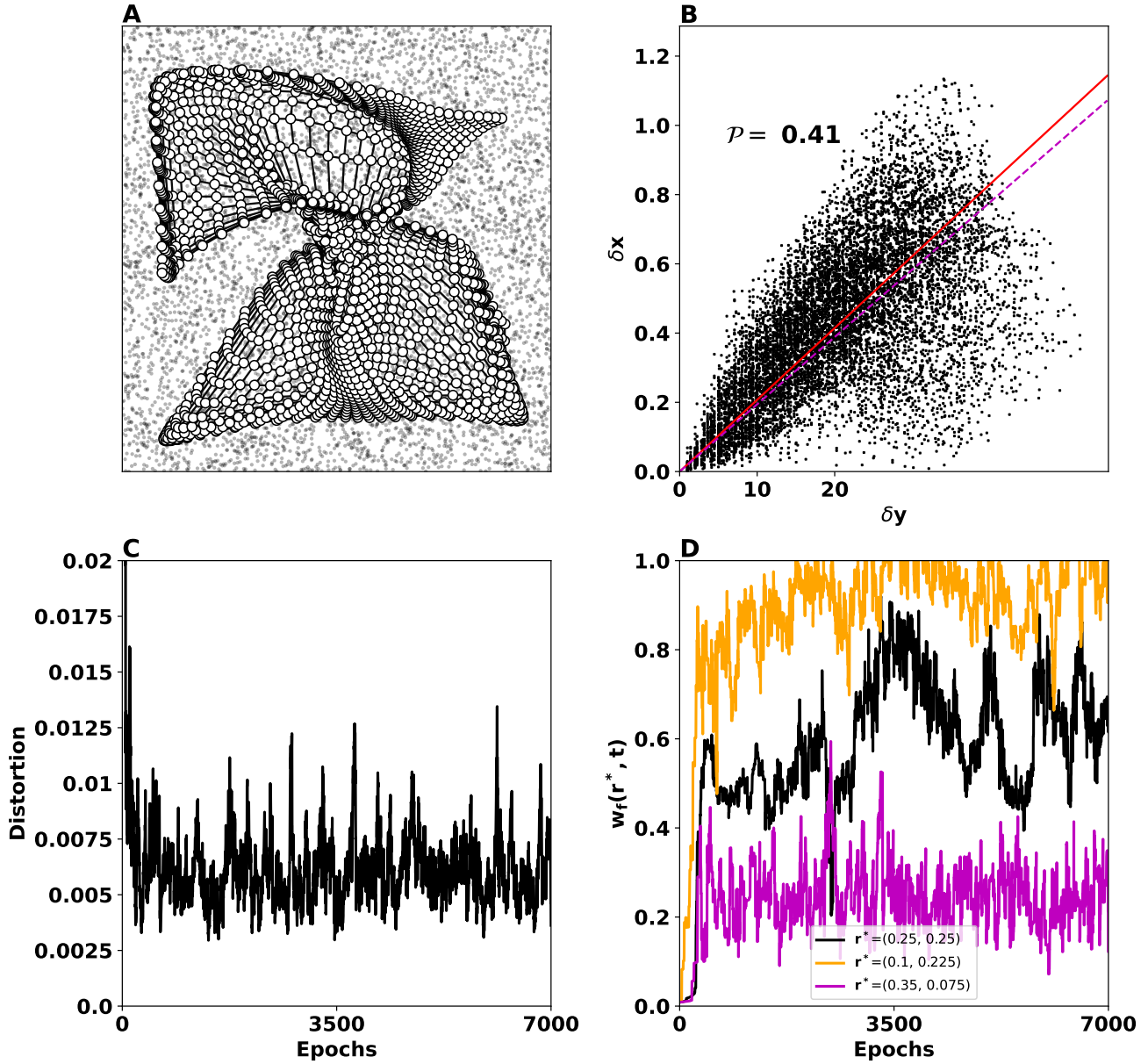


Figure 3: **Two-dimensional SOM performance in the unstable case.** **A** Feed-forward weights (white discs) as they have failed to organize into a topographic map after 7000 epochs. The input in this case is a two-dimensional rectangular uniform distribution (black dots). **B** $\delta x - \delta y$ representation (black cloud), mean of δx (red line), and the linear regression of the $\delta x - \delta y$ representation (magenta line). The fact that the cloud looks diffused indicates that the topographic map is not well-organized, as confirmed by a high value of $\mathcal{P} = 0.41$. **C** Distortion indicates that the loss of information during the learning process never drops (converges to an equilibrium) instead it oscillates. This means that the mapping of the input data to a two-dimensional map has failed. **D** Temporal evolution of norm-2 of feed-forward weights of three neurons placed at $r^* = (0.25, 0.25)$, $(0.1, 0.225)$, and $(0.35, 0.075)$). The condition (15) is violated and accordingly the weights do not converge to an equilibrium.

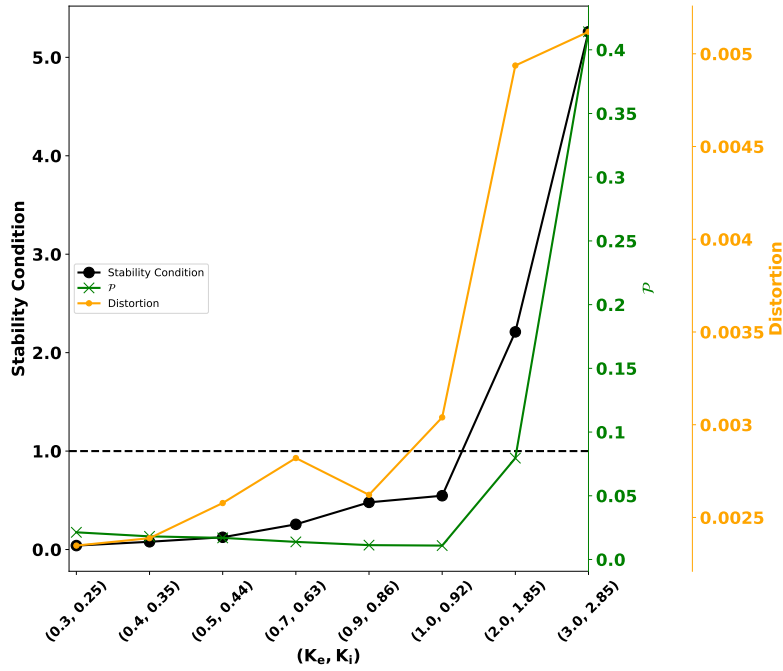


Figure 4: **Numerical investigation of Corollary 2.** Eight different pairs of the parameters (K_e, K_i) were used to investigate the conservativeness of the stability condition given by Corollary 2. We ran eight different simulations for 7000 epochs keeping always the rest of the parameters same as in Table 1 and the same PRNG seed as before (7659). The black curve indicates the numerical value of the left-hand side of (15): stability is guaranteed if it is below the black dashed line. The green curves indicates the $\delta x - \delta y$ performance index \mathcal{P} . The orange curve represents the distortion \mathcal{D} averaged of the 10 last epochs. It is apparent that as the values of (K_e, K_i) increase the Corollary 2 becomes violated and the self-organizing map is fails to map the input space to the neural one (see Figure 5 for more details).

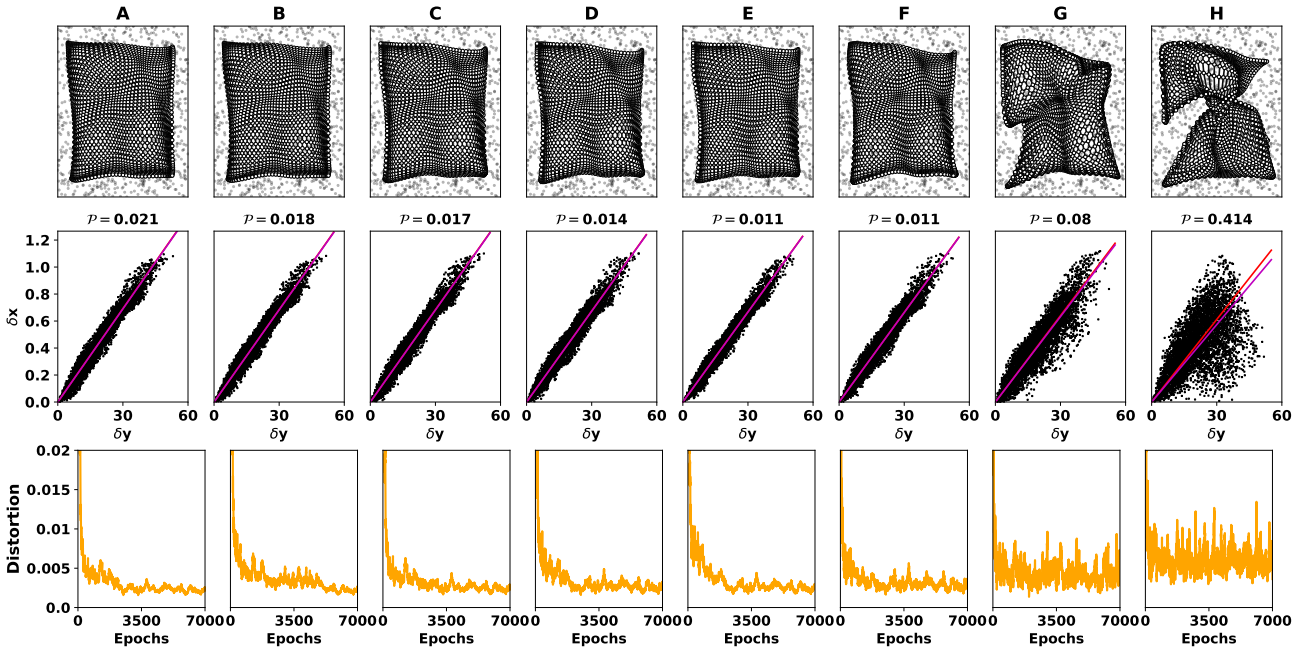


Figure 5: **Numerical Investigation of Corollary 2.** For the same eight experiments as in Figure 4, the obtained self-organizing map is provided (first line), together with its $\delta x - \delta y$ representation (second line) and the evolution of the distortion (third line). The mean δx is represented as a red line, whereas the slope of the linear regression is given as a magenta line. **A:** ($K_e = 0.30, K_i = 0.25$), **B:** ($K_e = 0.4, K_i = 0.35$), **C:** ($K_e = 0.5, K_i = 0.45$), **D:** ($K_e = 0.7, K_i = 0.63$), **E:** ($K_e = 0.9, K_i = 0.86$), **F:** ($K_e = 1.0, K_i = 0.92$). In line with Figure 4, a relevant map is obtained for the first five experiments (for which Condition (15) is fulfilled), whereas for the two last self-organizing maps **G:** ($K_e = 2, K_i = 1.85$), **H:** ($K_e = 3, K_i = 2.85$) the stability condition (15) is violated. This violation results in a non-stable neural field equation and thus the self-organizing maps do not learn properly the representations.

290 These stability conditions provide a means to identify the parameters set within which the unsupervised
 291 learning works efficiently, and thus provides an indication on how to tune them in practice. In particular,
 292 they can be used to further investigate how the dynamics of an underlying system affects the learning
 293 process during an unsupervised training process and what is the effect of the parameters on the final
 294 topographic map: as Figure 4 indicates, the parameters of the model directly affect the quality of
 295 the topographic map. However, a limitation of the present work is that it does not offer a way to
 296 choose the parameters in an optimal way. Furthermore, although the conditions provided by Theorem 1
 297 guarantee stability of the neural field, they do not predict the quality of the obtained map: stability
 298 ensures that the learning will converge to an equilibrium, but the quality of the obtained map strongly
 299 depends on the structure of this equilibrium, hence on the chosen initial values of the feed-forward
 300 weights. This is a well-known problem with self-organizing maps [19] that is generally solved using
 301 a decreasing neighborhood, starting from a very wide one. In our case, the neighborhood function
 302 is directly correlated with the profile of the field activity and is *fixed* (stereotyped). We thus cannot
 303 always ensure the proper unfolding of the map. It is to be noted that when the neighborhood of a
 304 Kohonen is kept fixed, it suffers from similar problems. Nevertheless, the numerical assessment of the
 305 proposed theoretical stability conditions suggest that the stability condition accurately predicts the
 306 emergence of topographic maps through unsupervised learning: see Figures 4 and 5.

307 Other works have studied stability conditions for Kohonen maps and vector quantization algorithms,
 308 using methods from linear systems stability theory [31] or through energy functions [?]. However, these
 309 works focus on the learning rule for the Kohonen self-organizing maps [20] and the dynamics are not
 310 explicitly given by dynamical systems. Our work goes beyond by taking into account not only the
 311 learning dynamics, but also the neural dynamics that drives the self-organizing process.

312 Last but not least, it has been shown that neural adaptation is crucial in the development of the
 313 neocortex [22] and neurons tend to adapt their input/output relation according to the statistics of the
 314 input stimuli. Our theoretical results provide conditions under which this input/output adaptation
 315 successfully takes place at least at a computational level.

316 6 Proof of the theoretical results

317 6.1 Proof of Theorem 1

In order to place the equilibrium at the origin, we employ the following change of variables:

$$\begin{aligned}\tilde{u}(r, t) &= u(r, t) - u^*(r) \\ \tilde{w}_f(r, t) &= w_f(r, t) - w_f^*(r),\end{aligned}$$

where u^* and w_f^* denote the equilibrium patterns of Eq. (6), as defined in Eq. (7). Then, the system (6) can be written as

$$\tau \frac{\partial \tilde{u}}{\partial t}(r, t) = -\tilde{u}(r, t) + \int_{\Omega} w_l(r, r') \tilde{f}_l(r', \tilde{u}(r', t)) dr' + \tilde{f}_s(\tilde{w}_f(r, t)) \quad (17a)$$

$$\frac{\partial \tilde{w}_f}{\partial t}(r, t) = -\gamma \tilde{w}_f(r, t) \int_{\Omega} w_e(r, r') \tilde{f}_e(\tilde{u}(r', t)) dr'. \quad (17b)$$

where, for all $x \in \mathbb{R}$ and all $r \in \Omega$,

$$\begin{aligned}\tilde{f}_l(r, x) &= f_l(x + u^*(r)) - f_l(u^*(r)) \\ \tilde{f}_s(x) &= f_s(x) - f_s(0) \\ \tilde{f}_e(r, x) &= f_e(x + u^*(r)).\end{aligned}$$

318 With this notation, it holds that $\tilde{f}_l(r, 0) = \tilde{f}_s(0) = 0$ for all $r \in \Omega$, meaning that (17) owns an
 319 equilibrium at zero. The stability properties of the origin of (17) thus determines those of the equilibria
 320 of (6).

First observe that, since w_e is a bounded function and Ω is compact, there exists $\bar{w}_e > 0$ such that

$$\int_{\Omega} w_e(r, r')^2 dr' \leq \bar{w}_e^2, \quad \forall r \in \Omega. \quad (18)$$

321

322 In order to assess the stability of (17), one may be tempted to rely on linearization techniques.
 323 Nevertheless, the linearized system (17) around the origin would necessarily involve the derivative of
 324 f_s at zero, which may be undefined if f_s is not differentiable at zero (which is the case for the system
 325 of interest (1)-(5) where f_s involves an absolute value). Consequently, the proof we propose here relies
 326 on Lyapunov methods [17] that were extended to neural fields in [10].

Consider the following Lyapunov functional:

$$V(t) := \frac{\tau}{2} \int_{\Omega} \tilde{u}(r, t)^2 dr + \frac{\rho}{2\gamma} \int_{\Omega} \tilde{w}_f(r, t)^2 dr, \quad (19)$$

where $\rho > 0$ denotes a parameter whose value will be decided later. First observe that the following bounds hold at all $t \geq 0$:

$$\underline{\alpha} \left(\|\tilde{u}(\cdot, t)\|^2 + \|\tilde{w}_f(\cdot, t)\|^2 \right) \leq V(t) \leq \bar{\alpha} \left(\|\tilde{u}(\cdot, t)\|^2 + \|\tilde{w}_f(\cdot, t)\|^2 \right), \quad (20)$$

where $\underline{\alpha} := \frac{1}{2} \min\{\tau; \rho/\gamma\} > 0$ and $\bar{\alpha} := \frac{1}{2} \max\{\tau; \rho/\gamma\} > 0$. The derivative of V along the solutions of (6) reads

$$\begin{aligned} \dot{V}(t) &= \tau \int_{\Omega} \tilde{u}(r, t) \frac{\partial \tilde{u}(r, t)}{\partial t} dr + \frac{\rho}{\gamma} \int_{\Omega} \tilde{w}_f(r, t) \frac{\partial \tilde{w}_f(r, t)}{\partial t} dr \\ &= \int_{\Omega} \tilde{u}(r, t) \left[-\tilde{u}(r, t) + \int_{\Omega} w_l(r, r') \tilde{f}_l(r', \tilde{u}(r', t)) dr' + \tilde{f}_s(\tilde{w}_f(r, t)) \right] dr \\ &\quad - \rho \int_{\Omega} \left[\tilde{w}_f(r, t)^2 \int_{\Omega} w_e(r, r') \tilde{f}_e(r', \tilde{u}(r', t)) dr' \right] dr. \end{aligned} \quad (21)$$

Moreover, denoting by ℓ_s , ℓ_e and ℓ_l the Lipschitz constants of f_s , f_e and f_l respectively, it holds that, for all $x \in \mathbb{R}$ and all $r \in \Omega$.

$$|\tilde{f}_l(r, x)| \leq \ell_l |x| \quad (22)$$

$$|\tilde{f}_s(x)| \leq \ell_s |x| \quad (23)$$

$$|\tilde{f}_e(r, x) - \tilde{f}_e(r, 0)| \leq \ell_e |x|. \quad (24)$$

Applying the Cauchy-Schwarz inequality and using Eq. (22), it follows that

$$\begin{aligned} \int_{\Omega} w_l(r, r') \tilde{f}_l(r', \tilde{u}(r', t)) dr' &\leq \int_{\Omega} |w_l(r, r')| |\tilde{f}_l(r', \tilde{u}(r', t))| dr' \\ &\leq \ell_l \int_{\Omega} |w_l(r, r')| |\tilde{u}(r', t)| dr' \\ &\leq \ell_l \sqrt{\int_{\Omega} w_l(r, r')^2 dr'} \sqrt{\int_{\Omega} \tilde{u}(r', t)^2 dr'}. \end{aligned}$$

Hence, using again Cauchy-Schwarz inequality,

$$\begin{aligned} &\int_{\Omega} \tilde{u}(r, t) \left[\int_{\Omega} w_l(r, r') \tilde{f}_l(r', \tilde{u}(r', t)) dr' \right] dr \\ &\leq \ell_l \int_{\Omega} |\tilde{u}(r, t)| \left[\sqrt{\int_{\Omega} w_l(r, r')^2 dr'} \sqrt{\int_{\Omega} \tilde{u}(r', t)^2 dr'} \right] dr \\ &\leq \ell_l \sqrt{\int_{\Omega} \tilde{u}(r, t)^2 dr} \sqrt{\int_{\Omega} \left[\int_{\Omega} w_l(r, r')^2 dr' \int_{\Omega} \tilde{u}(r', t)^2 dr' \right] dr}. \end{aligned}$$

Observing that $\int_{\Omega} \tilde{u}(r', t)^2 dr'$ is independent of r and defining

$$\bar{w}_l := \sqrt{\int_{\Omega} \int_{\Omega} w_l(r, r')^2 dr' dr}, \quad (25)$$

it follows that

$$\int_{\Omega} \tilde{u}(r, t) \left[\int_{\Omega} w_l(r, r') \tilde{f}_l(r', \tilde{u}(r', t)) dr' \right] dr \leq \ell_l \bar{w}_l \int_{\Omega} \tilde{u}(r, t)^2 dr. \quad (26)$$

Furthermore, using Eq. (23), we have that

$$\begin{aligned} \int_{\Omega} \tilde{u}(r, t) \tilde{f}_s(w_f(r, t)) dr &\leq \ell_s \int_{\Omega} |\tilde{u}(r, t)| |w_f(r, t)| dr \\ &\leq \ell_s \sqrt{\int_{\Omega} \tilde{u}(r, t)^2 dr} \sqrt{\int_{\Omega} w_f(r, t)^2 dr} \end{aligned}$$

Invoking the inequality $2ab \leq (a^2/\lambda + \lambda b^2)$ for all $a, b \in \mathbb{R}$ and all $\lambda > 0$, we obtain that

$$\int_{\Omega} \tilde{u}(r, t) \tilde{f}_s(\tilde{w}_f(r, t)) dr \leq \frac{\ell_s}{2} \left(\lambda \int_{\Omega} \tilde{u}(r, t)^2 dr + \frac{1}{\lambda} \int_{\Omega} \tilde{w}_f(r, t)^2 dr \right), \quad (27)$$

327 for any $\lambda > 0$.

Now, assumption (10) ensures that $\inf_{r \in \Omega} \int_{\Omega} w_e(r, r') \tilde{f}_e(r', 0) dr' > 0$. It follows that there exists $c > 0$ such that

$$\int_{\Omega} w_e(r, r') \tilde{f}_e(r', 0) dr' \geq 2c, \quad \forall r \in \Omega.$$

Consequently, using (24) and Cauchy-Schwarz inequality, we get that, for any $v \in L_2(\Omega, \mathbb{R})$,

$$\begin{aligned} \int_{\Omega} w_e(r, r') \tilde{f}_e(r', v(r')) dr' &= \int_{\Omega} w_e(r, r') \tilde{f}_e(r', 0) dr' + \int_{\Omega} w_e(r, r') (\tilde{f}_e(r', v(r')) - \tilde{f}_e(r', 0)) dr' \\ &\geq 2c - \int_{\Omega} |w_e(r, r')| |\tilde{f}_e(r', v(r')) - \tilde{f}_e(r', 0)| dr' \\ &\geq 2c - \ell_e \int_{\Omega} |w_e(r, r')| |v(r')| dr' \\ &\geq 2c - \ell_e \sqrt{\int_{\Omega} w_e(r, r')^2 dr'} \sqrt{\int_{\Omega} v(r')^2 dr'} \\ &\geq 2c - \ell_e \bar{w}_e \|v\|, \end{aligned}$$

where the last bound comes from (18). Let \mathcal{B}_ε denote the ball (in L_2 -norm) of radius $\varepsilon > 0$, that is: $\mathcal{B}_\varepsilon := \{v \in L_2(\Omega, \mathbb{R}) : \|v\| < \varepsilon\}$. Letting $\varepsilon := c/\ell_e \bar{w}_e$, we conclude from the above expression that

$$\int_{\Omega} w_e(r, r') \tilde{f}_e(r', v(r')) dr' \geq c, \quad \forall r \in \Omega, \forall v \in \mathcal{B}_\varepsilon. \quad (28)$$

Consider an initial condition such that $\tilde{u}(\cdot, 0) \in \mathcal{B}_\varepsilon$ and let $T \in [0, +\infty]$ denote the time needed for $\tilde{u}(\cdot, t)$ to leave \mathcal{B}_ε . Then it holds by definition that $\tilde{u}(\cdot, t) \in \mathcal{B}_\varepsilon$ for all $t \in [0, T)$ and $\tilde{u}(\cdot, T) \notin \mathcal{B}_\varepsilon$ if T is finite. Note that, by continuity of solutions, $T > 0$. Moreover, in view of (28),

$$\int_{\Omega} w_e(r, r') \tilde{f}_e(r', \tilde{u}(r', t)) dr' \geq c, \quad \forall t \in [0, T), \forall r \in \Omega. \quad (29)$$

Combining Eq.(21), (22), (23), and (29), we obtain that, for all $t \in [0, T)$,

$$\dot{V}(t) \leq - \left(1 - \ell_l \bar{w}_l - \frac{\lambda \ell_s}{2} \right) \int_{\Omega} \tilde{u}(r, t)^2 dr - \left(\rho c - \frac{\ell_s}{2\lambda} \right) \int_{\Omega} \tilde{w}_f(r, t)^2 dr$$

Pick $\lambda = (1 - \ell_l \bar{w}_l) / \ell_s$. Note that $\lambda > 0$ since $\ell_l \bar{w}_l < 1$ by assumption (see Eq. (9)). Then the choice $\rho = \frac{\ell_s}{c\lambda} = \frac{\ell_s^2}{c(1 - \ell_l \bar{w}_l)} > 0$ leads to:

$$\begin{aligned} \dot{V}(t) &\leq -\frac{1}{2} \|\tilde{u}(\cdot, t)\|^2 - \frac{\rho c}{2} \|\tilde{w}_f(\cdot, t)\|^2 \\ &\leq -\frac{1}{2} \min\{1; \rho c\} \left(\|\tilde{u}(\cdot, t)\|^2 + \|\tilde{w}_f(\cdot, t)\|^2 \right). \end{aligned}$$

Using (20) and letting $\alpha := \frac{1}{2\bar{\alpha}} \min\{1; \rho c\} > 0$, we finally obtain that

$$\dot{V}(t) \leq -\alpha V(t), \quad \forall t \in [0, T).$$

Integrating, this gives $V(t) \leq V(0)e^{-\alpha t}$ for all $t \in [0, T)$, which yields, using (20),

$$\|\tilde{u}(\cdot, t)\|^2 + \|\tilde{w}_f(\cdot, t)\|^2 \leq \frac{\bar{\alpha}}{\underline{\alpha}} \left(\|\tilde{u}(\cdot, 0)\|^2 + \|\tilde{w}_f(\cdot, 0)\|^2 \right) e^{-\alpha t}, \quad \forall t \in [0, T). \quad (30)$$

Thus, if initial conditions are picked within the L_2 -ball of radius $\frac{\sqrt{\bar{\alpha}}}{\varepsilon\sqrt{\underline{\alpha}}}$, then $\|\tilde{u}(\cdot, t)\| + \|\tilde{w}_f(\cdot, t)\| < \varepsilon$ at all times $t \geq 0$. This means that, for these initial conditions, solutions never leave the ball \mathcal{B}_ε , hence $T = +\infty$. Eq. (30) thus ensures exponential stability on this set of initial conditions.

6.2 Proof of Corollary 1

Assumption described by Eq. (13) is equivalent to requiring $\bar{w}_l < 1$, with \bar{w}_l defined in Eq. (25). Since the Lipschitz constant of the rectification is $\ell_l = 1$, this makes Eq. (9) fulfilled.

Moreover, we claim that the solution u^* of the implicit Eq. (12) is necessarily positive on some subset of Ω with non-zero measure. To see this, assume on contrary that $u^*(r) \leq 0$ for almost all $r \in \Omega$. Then it holds that $\text{rect}(u^*(r)) = 0$ for almost all $r \in \Omega$, which implies that

$$\int_{\Omega} w_l(r, r') \text{rect}(u^*(r')) dr' = 0, \quad \forall r \in \Omega.$$

In view of Eq. (12), this implies that $u^*(r) = 1$ for all $r \in \Omega$, thus leading to a contradiction. Consequently, as claimed, u^* is necessarily positive on some subset Ω^+ of Ω with non-zero measure. Recalling that Ω is here assumed to be a compact set, it follows that

$$\inf_{r \in \Omega} \int_{\Omega} e^{-|r-r'|^2/2\sigma_e^2} \text{rect}(u^*(r)) dr \geq \inf_{r \in \Omega} \int_{\Omega^+} e^{-|r-r'|^2/2\sigma_e^2} u^*(r) dr > 0,$$

which makes Eq. (10) satisfied. The conclusion then follows from Theorem 1.

6.3 Proof of Corollary 2

The following one-dimensional relation holds:

$$\int_a^b \int_a^b e^{-\frac{|x-y|^2}{2\sigma^2}} dx dy = \sqrt{\xi_{a,b}(\sigma)}. \quad (31)$$

In order to compute its two-dimensional counterpart, let $r = (r_1, r_2)$ and $r' = (r'_1, r'_2)$. Then, for $\Omega = [a, b] \times [a, b]$,

$$\int_{\Omega} \int_{\Omega} e^{-\frac{|r-r'|^2}{2\sigma^2}} dr' dr = \int_a^b \int_a^b \int_a^b \int_a^b \exp\left(-\frac{(r_1 - r'_1)^2 + (r_2 - r'_2)^2}{2\sigma^2}\right) dr'_1 dr'_2 dr_1 dr_2.$$

Using Fubini's theorem, it follows that

$$\int_{\Omega} \int_{\Omega} e^{-\frac{|r-r'|^2}{2\sigma^2}} dr' dr = \int_a^b \int_a^b \exp\left(-\frac{(r_1 - r'_1)^2}{2\sigma^2}\right) \left(\int_a^b \int_a^b \exp\left(-\frac{(r_2 - r'_2)^2}{2\sigma^2}\right) dr_2 dr'_2 \right) dr_1 dr'_1$$

From Eq. (31), this gives:

$$\begin{aligned} \int_{\Omega} \int_{\Omega} e^{-\frac{|r-r'|^2}{2\sigma^2}} dr' dr &= \int_a^b \int_a^b \exp\left(-\frac{(r_1 - r'_1)^2}{2\sigma^2}\right) \sqrt{\xi_{a,b}(\sigma)} dr_1 dr'_1 \\ &= \xi_{a,b}(\sigma). \end{aligned} \quad (32)$$

The left-hand term of Eq. (13) then reads:

$$\begin{aligned} \int_{\Omega} \int_{\Omega} \left(K_e e^{-\frac{|r-r'|^2}{2\sigma_e^2}} - K_i e^{-\frac{|r-r'|^2}{2\sigma_i^2}} \right)^2 dr' dr &= \int_{\Omega} \int_{\Omega} \left(K_e^2 e^{-\frac{|r-r'|^2}{\sigma_e^2}} + K_i^2 e^{-\frac{|r-r'|^2}{\sigma_i^2}} - 2K_e K_i e^{-\frac{|r-r'|^2 \sigma_e \sigma_i}{2\sqrt{\sigma_e^2 + \sigma_i^2}}} \right) dr' dr \\ &= K_e^2 \xi_{a,b}(\sigma_e/\sqrt{2}) + K_i^2 \xi_{a,b}(\sigma_i/\sqrt{2}) - 2K_e K_i \xi_{a,b} \left(\frac{\sigma_e \sigma_i}{\sqrt{\sigma_e^2 + \sigma_i^2}} \right), \end{aligned}$$

336 which concludes the proof.

337 PRNG Seed

338 We ran both the stable and non-stable experiments ten times with different PRNG seeds. All the
339 PRNG seeds we used are: 10, 74, 433, 721, 977, 1330, 3433, 5677, 9127, 7659.

340 Acknowledgments

341 Not applicable.

342 Funding

343 This work was partially funded by grant ANR-17-CE24-0036.

344 Abbreviations

345 **SOM** Self-organizing Map

346 **DSOM** Dynamic Self-organizing Map

347 **FFT** Fast Fourier Transform

348 **PRNG** Pseudo Random Number Generator

349 Availability of data and materials

350 The source code used in this work for running the simulations, analysing the results and plotting the
351 figures, is freely distributed under the GPL-3 License and can be found here: https://github.com/gdeter/som_stability.
352

353 Ethics approval and consent to participate

354 Not applicable.

355 Competing interests

356 All three authors declare that the research was conducted in the absence of any commercial or financial
357 relationships that could be construed as a potential conflict of interest.

358 Consent for publication

359 Not applicable.

360 Author's contributions

361 GID conceived the idea, wrote the code, designed and ran the numerical experiments, AC performed
362 the mathematical derivation and analysis. GID, AC, and NPR contributed to preparing, writing, and
363 revising the manuscript.

364 References

- 365 [1] Larry F Abbott and Sacha B Nelson. Synaptic plasticity: taming the beast. *Nature neuroscience*,
366 3:1178–1183, 2000.
- 367 [2] M. Abramowitz and I.A. Stegun. *Handbook of Mathematical Functions with Formula, Graphs and*
368 *Mathematical Tables*. Dover Publications, 1983.
- 369 [3] S. Amari. Dynamics of pattern formation in lateral-inhibition type neural fields. *Biological*
370 *cybernetics*, 27(2):77–87, 1977.
- 371 [4] Paul C Bressloff. Spatiotemporal dynamics of continuum neural fields. *Journal of Physics A:*
372 *Mathematical and Theoretical*, 45(3):033001, 2012.
- 373 [5] S. Coombes. Waves, bumps, and patterns in neural field theories. *Biological Cybernetics*, 93(2):91–
374 108, 2005.
- 375 [6] Thomas M Cover and Joy A Thomas. *Elements of information theory*. John Wiley & Sons, 2012.
- 376 [7] Pierre Demartines. Organization measures and representations of kohonen maps. In *First IFIP*
377 *Working Group*, volume 10. Citeseer, 1992.
- 378 [8] Georgios Is Detorakis and Nicolas P Rougier. A neural field model of the somatosensory cortex:
379 formation, maintenance and reorganization of ordered topographic maps. *PloS one*, 7(7):e40257,
380 2012.
- 381 [9] Georgios Is Detorakis and Nicolas P Rougier. Structure of receptive fields in a computational
382 model of area 3b of primary sensory cortex. *Frontiers in Computational Neuroscience*, 8(76), 2014.
- 383 [10] Olivier Faugeras, François Grimbert, and Jean-Jacques Slotine. Absolute stability and complete
384 synchronization in a class of neural fields models. *SIAM Journal on Applied Mathematics*,
385 69(1):205–250, 2008.
- 386 [11] Olivier Faugeras, Romain Veltz, and François Grimbert. Persistent neural states: stationary
387 localized activity patterns in nonlinear continuous n-population, q-dimensional neural networks.
388 *Neural computation*, 21(1):147–187, 2009.
- 389 [12] Mathieu N Galtier, Olivier D Faugeras, and Paul C Bressloff. Hebbian learning of recurrent
390 connections: a geometrical perspective. *Neural computation*, 24(9):2346–2383, 2012.
- 391 [13] Kamil A Grajski and Michael Merzenich. Neural network simulation of somatosensory rep-
392 resentational plasticity. In *Advances in neural information processing systems*, pages 52–59,
393 1990.
- 394 [14] Stephen Grossberg. Physiological interpretation of the self-organizing map algorithm. 1994.
- 395 [15] Donald Olding Hebb. *The organization of behavior: A neuropsychological theory*. Psychology
396 Press, 2002.
- 397 [16] Samuel Kaski, Jari Kangas, and Teuvo Kohonen. Bibliography of self-organizing map (som)
398 papers: 1981–1997. *Neural computing surveys*, 1(3&4):1–176, 1998.

- 399 [17] H. Khalil. *Nonlinear systems*. Macmillan Publishing Co., 2nd ed., New York, 1996.
- 400 [18] Robert T Knight, W Richard Staines, Diane Swick, and Linda L Chao. Prefrontal cortex regulates
401 inhibition and excitation in distributed neural networks. *Acta psychologica*, 101(2):159–178, 1999.
- 402 [19] Teuvo Kohonen. Self-organized formation of topologically correct feature maps. *Biological*
403 *cybernetics*, 43(1):59–69, 1982.
- 404 [20] Teuvo Kohonen. *Self-organizing maps*, volume 30. Springer, 2001.
- 405 [21] Leah A Krubitzer and Jon H Kaas. The organization and connections of somatosensory cortex in
406 marmosets. *The Journal of Neuroscience*, 10(3):952–974, 1990.
- 407 [22] Rebecca A Mease, Michael Famulare, Julijana Gjorgjieva, William J Moody, and Adrienne L
408 Fairhall. Emergence of adaptive computation by single neurons in the developing cortex. *The*
409 *Journal of Neuroscience*, 33(30):12154–12170, 2013.
- 410 [23] Risto Miikkulainen, James A Bednar, Yoonsuck Choe, and Joseph Sirosh. *Computational maps in*
411 *the visual cortex*. Springer Science & Business Media, 2006.
- 412 [24] Nasser M Nasrabadi and Yushu Feng. Vector quantization of images based upon the kohonen
413 self-organizing feature maps. In *Proc. IEEE Int. Conf. Neural Networks*, volume 1, pages 101–105,
414 1988.
- 415 [25] Erkki Oja. Simplified neuron model as a principal component analyzer. *Journal of mathematical*
416 *biology*, 15(3):267–273, 1982.
- 417 [26] Merja Oja, Samuel Kaski, and Teuvo Kohonen. Bibliography of self-organizing map (som) papers:
418 1998-2001 addendum. *Neural computing surveys*, 3(1):1–156, 2003.
- 419 [27] HX Qi, TM Preuss, and JH Kaas. Somatosensory areas of the cerebral cortex: architectonic
420 characteristics and modular organization. *The senses: A comprehensive reference*, 6:143, 2008.
- 421 [28] Nicolas Rougier and Yann Boniface. Dynamic self-organising map. *Neurocomputing*, 74(11):1840–
422 1847, 2011.
- 423 [29] Michael Schaefer, Hans-Jochen Heinze, and Michael Rotte. Task-relevant modulation of primary
424 somatosensory cortex suggests a prefrontal–cortical sensory gating system. *Neuroimage*, 27(1):130–
425 135, 2005.
- 426 [30] Joseph Sirosh and Risto Miikkulainen. Ocular dominance and patterned lateral connections in a
427 self-organizing model of the primary visual cortex. *Advances in Neural Information Processing*
428 *Systems*, pages 109–116, 1995.
- 429 [31] Mauro Tucci and Marco Raugi. Stability analysis of self-organizing maps and vector quantization
430 algorithms. In *The 2010 International Joint Conference on Neural Networks (IJCNN)*, pages 1–5.
431 IEEE, 2010.
- 432 [32] Romain Veltz and Olivier Faugeras. Local/global analysis of the stationary solutions of some
433 neural field equations. *SIAM Journal on Applied Dynamical Systems*, 9(3):954–998, 2010.
- 434 [33] Stuart P Wilson, Judith S Law, Ben Mitchinson, Tony J Prescott, and James A Bednar. Modeling
435 the emergence of whisker direction maps in rat barrel cortex. *PloS one*, 5(1):e8778, 2010.
- 436 [34] Jing Xing and George L Gerstein. Networks with lateral connectivity. i. dynamic properties
437 mediated by the balance of intrinsic excitation and inhibition. *Journal of neurophysiology*,
438 75(1):184–199, 1996.
- 439 [35] Jing Xing and George L Gerstein. Networks with lateral connectivity. ii. development of neuronal
440 grouping and corresponding receptive field changes. *Journal of neurophysiology*, 75(1):200–216,
441 1996.

- 442 [36] Jing Xing and George L Gerstein. Networks with lateral connectivity. iii. plasticity and reorgani-
443 zation of somatosensory cortex. *Journal of neurophysiology*, 75(1):217–232, 1996.
- 444 [37] Hujun Yin. Learning nonlinear principal manifolds by self-organising maps. In *Principal manifolds*
445 *for data visualization and dimension reduction*, pages 68–95. Springer, 2008.